The Planetary Science Journal, 3:17 (15pp), 2022 January https://doi.org/10.3847/PSJ/ac4501

Radial Distribution of the Dust Comae of Comets 45P/Honda–Mrkos–Pajdušáková and 46P/Wirtanen

C. Lejoly[1], W. Harris[1], N. Samarasinha[2], B. E. A. Mueller[2], E. Howell[1], J. Bodnarik[1], A. Springmann[1], T. Kareta[1], B. Sharkey[1], J. Noonan[1]
(4*P Campaign),
L. R. Bedin[3], J.-G. Bosch[4,18], A. Brosio[5], E. Bryssinck[6,7,8,19,20], J.-B. de Vanssay[4,18], F.-J. Hambsch[7,9,20], O. Ivanova[10,11,12], V. Krushinsky[13], Z.-Y. Lin[14], F. Manzini[15], A. Maury[4,18], N. Moriya[16], P. Ochner[3,17], and V. Oldani[15]
[1] Lunar and Planetary Laboratory, 1629 E University Boulevard, Tucson, AZ 85721-0092, USA
[2] Planetary Science Institute, 1700 East Fort Lowell, Suite 106, Tucson, AZ 85719-2395, USA
[3] INAF—Osservatorio Astronomica di Padova, Vicolo dell'Osservatorio 5, I-35122, Padova, Italy
[4] SpaceObs, San Pedro de Atacama, Chile
[5] L'osservatorio Astronomico di Savelli, Via Villaggio Pino Grande (SP 28), Località Timpa Caccianinni, I-88825, Savelli (KR), Italy
[6] CARA Consortium (Cometary ARchive for Afrho), Italy
[7] Vereniging Voor Sterrenkunde (VVS), Oostmeers 122 C, B-8000 Brugge, Belgium
[8] The British Astronomical Association (BAA), Burlington House, Piccadilly, London, W1J 0DU, UK
[9] American Association of Variable Star Observers (AAVSO), 49 Bay State Road, Cambridge, MA 02138, USA
[10] Astronomical Institute of the Slovak Academy of Sciences, Slovakia
[11] Main Astronomical Observatory of the National Academy of Sciences of Ukraine, Ukraine
[12] Taras Shevchenko National University of Kyiv, Astronomical Observatory, Ukraine
[13] Laboratory of Astrochemical Research, Ural Federal University, Ekaterinburg, Russia, ul. Mira d. 19, Yekaterinburg, 620002, Russia
[14] National Central University, No. 300, Zhongda Road, Zhongli District, Taoyuan City 32001, Taiwan, Republic of China
[15] Stazione Astronomica di Sozzago, I-28060 Sozzago (Novara), Italy
[16] siOnet Ltd.—Applied Modeling Research, Faran Observatory, Mitzpe-Ramon, Negev 47113, Israel
[17] Dept. of Physics and Astronomy, University of Padova, Via Marzolo 8, I-35131 Padova, Italy
Received 2021 July 29; revised 2021 December 13; accepted 2021 December 18; published 2022 January 24

Abstract

There was an unprecedented opportunity to study the inner dust coma environments, where the dust and gas are not entirely decoupled, of comets 45P/Honda–Mrkos–Pajdušáková (45P/HMP) from 2016 December 26 to 2017 March 15, and 46P/Wirtanen from 2018 November 10 to 2019 February 13, both in visible wavelengths. The radial profile slopes of these comets were measured in the *R* and HB-BC filters most representative of dust, and deviations from a radially expanding coma were identified as significant. The azimuthally averaged radial profile slope of comet 45P/HMP gradually changes from -1.81 ± 0.20 at 5.24 days preperihelion to -0.35 ± 0.16 at 74.41 days postperihelion. Contrastingly, the radial profile slope of 46P/Wirtanen stays fairly constant over the observed time period at -1.05 ± 0.05. Additionally, we find that the radial profile of 46P/Wirtanen is azimuthally dependent on the sky-plane-projected solar position angle, while that of 45P/HMP is not. These results suggest that comets 45P/HMP and 46P/Wirtanen have vastly different coma dust environments and that their dust expansion properties are distinct. As evident from these two comets, well-resolved inner comae are vital for detailed characterization of dust environments.

Unified Astronomy Thesaurus concepts: Coma dust (2159); Comae (271); Short period comets (1452); Comets (280)

1. Introduction

From 2016 to 2019, there was an unique opportunity to study the dust and gas environment in the inner coma—typically defined as several thousand kilometers from the nucleus—of three closely approaching comets, 41P/Tuttle–Giacobini–Kresàk, 45P/Honda–Mrkos–Pajdušáková (45P/HMP), and 46P/Wirtanen. In this paper, we focus on the latter two comets. Both comets 45P/HMP and 46P/Wirtanen approached Earth to within 0.08 au, and were well placed for observational study. The close approach of these Jupiter family comets (JFCs) allowed for high spatial resolutions of the inner comae, which is a region typically not well resolved except by spacecraft or during the rare occasions when a comet has a close encounter with Earth. The proximity we obtain for these comets simply due to their orbits' close approach to Earth might not resolve them quite as well as a close flyby or in-situ study, but does provide a much more in-depth opportunity, without requiring the typical cost of a spacecraft mission. Table 1 shows the heliocentric and geocentric distance ranges, and the perihelion and perigee distances for our observation spans (JPL Solar System Dynamic Group 2021).

Comet 45P/HMP is a JFC with a perihelion distance of 0.53 au and an orbital period of 5.25 yr. It was found to have a radius of 0.60–0.65 km and a rotation period of ~7.5 hr (Lejoly & Howell 2017). Comet 46P/Wirtanen is also a JFC, with an orbital period of 5.4 yr and a perihelion distance of 1 au. It had a close approach to Earth on 2018 December 16 at 0.08 au and

[18] https://www.spaceobs.com
[19] http://cara.uai.it/home
[20] https://www.vvs.be

Table 1
Geometric Parameters for Comets 45P/HMP and 46P/Wirtanen

Comet	Perihelion Date and Time (UT)	Perihelion Distance (au)	r[a] (au)	Perigee Date (UT)	Perigee Distance (au)	Δ[b] (au)
45P/HMP	2016-12-31 06:29	0.53	−0.54 → 1.43	2017-02-11 7:03	0.08	−0.82 → 0.47
46P/Wirtanen	2018-12-12 22:20	1.06	−1.14 → 1.34	2018-12-16 2:10	0.08	−0.22 → 0.41

Notes. For the heliocentric and geocentric distances for our observations, negative values mean preperihelion/perigee. The individual observations are provided in Tables 3 and 4.
[a] Heliocentric range.
[b] Geocentric range.

was well placed for long-term monitoring from ground-based observatories. With its small radius of 0.6 km (Lamy et al. 1998), comet 46P/Wirtanen has been described as an hyperactive comet, meaning that its activity level is higher than its expected active fraction of the nucleus. Farnham et al. (2021) found that it had a period of around 9 hr during its 2018 passage.

1.1. Cometary Dust

Cometary dust is defined as an "unequilibrated, heterogeneous mixture of minerals, including both high- and low-temperature condensates" (Hanner & Bradley 2004) that does not typically sublimate upon close approach to the Sun, but that can be dragged along with the sublimating gases. Cometary dust is a primordial part of a comet, being mostly unaltered particles containing both presolar grains and solar nebula condensates. Additionally, the Stardust mission, which brought samples back from the coma of comet 81P/Wild 2, detected calcium aluminum-rich inclusions, suggesting some cometary dust was created in a hot protoplanetary disk (Brownlee 2014). Cometary dust measurements show a mixture of rock-forming elements, such as Mg, Si, Ca, Fe, and lighter elements, known as CHON particles (carbon, hydrogen, oxygen, and nitrogen; Hanner & Bradley 2004). Both crystalline and noncrystalline silicates are present; the major fraction of noncrystalline silicates is constituted of glassy silicate grains (glass with embedded metals and sulfides; GEMS). In-situ measurements of 67P/Churyumov–Gerasimenko show many organics and, in particular, phosphorus, which is an important element in the emergence of life (Altwegg et al. 2016). Cometary grains can be of any range of mixture from pure silicate to almost fully icy grains, and vary depending on the comet.

Cometary nuclei are often characterized as either icy "dirtballs" or dusty "snowballs" (Weissman et al. 2004). There are no definite composition models that fit every cometary nucleus; however, it can be inferred that a majority of cometary nuclei are collisionally processed rubble piles, defined as "primordial rubble piles that have subsequently undergone collisional evolution" (Weissman et al. 2004), "a 'layered-pile' model, in which the interior consists of a core overlain [sic] by a pile of randomly stacked layers" (Belton et al. 2006), or are a collection of coalesced smaller bodies if they were formed in a streaming instability (Weissman et al. 2020). The composition, porosity, and size distribution of particles within the inner coma, if originating directly from the inside of the nucleus, can shed light on the makeup of the cometary nucleus or, if originating from the upper layers of the cometary nucleus, can shed light on the evolution of cometary nuclei in general.

When being dragged through the coma, cometary dust particles can undergo several different processes, including grain lofting and grain fragmentation, which, if mixed with ice, create an icy-grain halo. As Figure 1 shows, grain lofting simply refers to gas-drag forces propelling dust particles from the surface of the nucleus and bringing it along to the coma. During the grain lofting process, the dust is accelerated by the gas until the gas density becomes so small that the acceleration is negligible, and the dust becomes decoupled from the gas. This region of decoupling usually defines the difference between the inner and outer coma and occurs around several thousand of kilometers and primarily depends on the gas-production rates.

Grain fragmentation occurs when large particles are broken up due to their "fluffy aggregate" structure. Grain fragmentation creates a change in observable dust reflective surface area from the simple grain-lofting model. An icy-grain halo is created when larger particles of dust and ice are lofted, then partially sublimate. The partial sublimation typically causes a depletion in the observable grain surface area. Both grain fragmentation and icy-grain halo have been analytically replicated by Markkanen & Agarwal (2020). It is important to understand that there are many additional processes under which cometary dust grains can evolve in the inner coma, and that the apparent radial distribution depends on a number of factors that come down to whether the cross-section, albedo, size distribution, and velocity distribution of the grains remain unchanged or not. Understanding the composition and structure of cometary dust allows us to remotely probe each individual cometary nucleus.

1.2. Fountain Model

As explained in Section 1.1, it is assumed that gases leaving the nucleus accelerate away due to gas expansion, among other forces. Solar radiation pressure effects are more apparent farther out from the nucleus and, following the equation of motion, the displacement caused by radiation pressure is proportional to the time it is exposed to the radiation field squared. During their sublimation, gases can pick up dust particles on the surface of the cometary nucleus and entrain them, in a process called grain lofting, as they move away from the nucleus until they are decoupled from the gas. At this point, if other dust processes are negligible, the dust particles usually expand radially at a constant velocity until they are affected by solar radiation pressure. This is the idea for the fountain model, as described by Eddington (1910). Although there is some evolution of the radial dust outflow in all directions, with dust grains accelerating due to radiation pressures, our paper focuses on the inner coma, where the decoupling from the gas occurs, but where the radiation pressure is not yet a major factor. Essentially, the inner coma is the location where the dust transitions from being coupled with the gas to being decoupled from the gas. A spherically expanding dust coma at a constant speed that is decoupled from the gas but is essentially

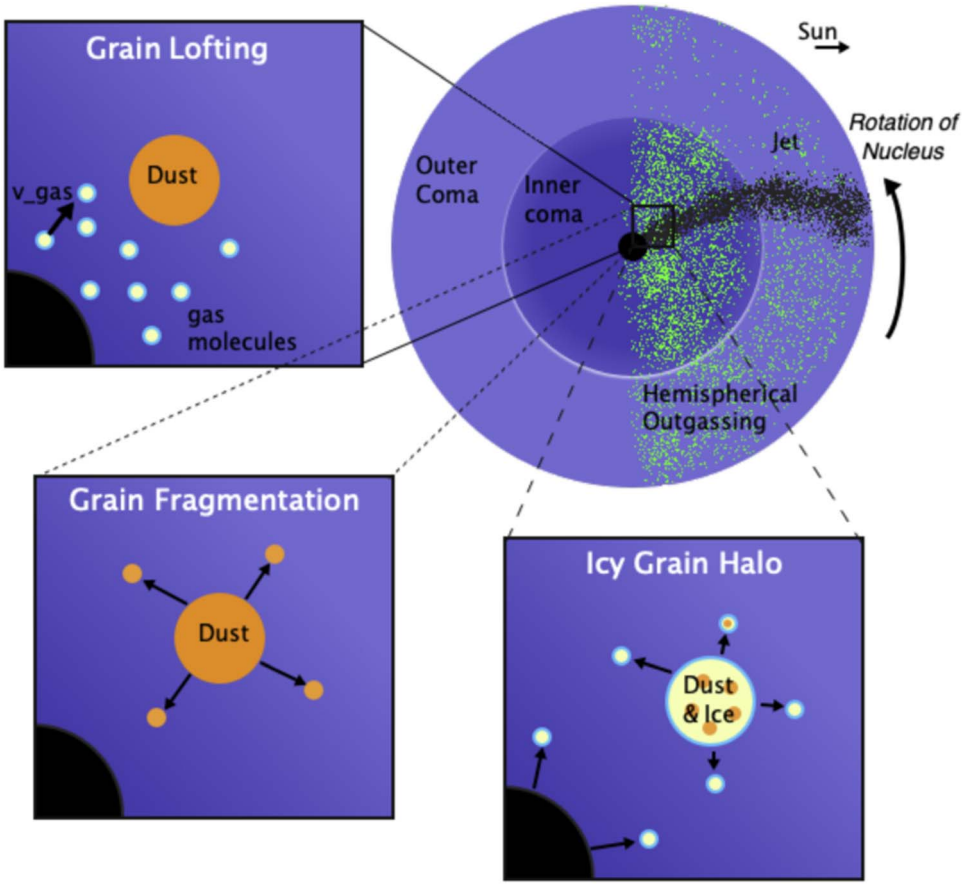

Figure 1. Cometary dust undergoes many changes in the coma. The relevant processes include grain lofting, grain fragmentation, formation of icy-grain halos, hemispherical outgassing, and jet features, which can be curved due to rotation of the nucleus.

unaffected by radiation pressure, when projected onto the plane perpendicular to the line of sight of the observer (sky plane), will produce a brightness profile proportional to $1/\rho$, where ρ is the projected distance from the nucleus on the sky plane.

Even though the fountain model has been known for over a hundred years, and has often been referenced when looking at cometary dust expansion, it is important to keep in mind that the expanding gas coma, which drags the dust with it, is composed of different gases that have a range of photodissociative lifetimes. Photodissociation of molecules will cause gas accelerations that may or may not occur within the region where dust and gas are coupled. The Haser (Haser 1957) and vectorial (Festou 1981) models represent the gas expansion in comae. Additionally, even if the dust and gas typically decouple within thousands of kilometers from the nucleus, the actual decoupling distance will depend on the shape and size of the dust particles (Ivanovski et al. 2017) in addition to the gas-production rate. Our ability to resolve the inner coma where the dust and gas might not yet be fully decoupled allows us to investigate the radial profile behavior of the dust comae, informing us of the grain environment.

2. Data

As seen in Table 1, images were obtained for a large range of geocentric and heliocentric distances. The exposure times were determined to match a nonsaturating nucleus, if nonsidereal tracking was available, otherwise the exposure times were optimized to avoid smearing. Images were obtained for the majority of the comets' observability in the sky for each night we had telescope time, and were on a repeating cycle through the observation campaign's set of filters. The differences in total observing nights available were impacted by the comets' geometry, the weather, and the telescopes' scheduling. It is important to note that 45P/HMP's limited observable window due to the observing geometry resulted in a smaller data set. A sample image for each comet, when closest to perihelion, is shown in Figure 2.

2.1. Telescopes

As shown in Table 2, the data presented here were obtained from multiple telescopes. We obtained the majority of our data for both comets with the 1.54 m Kuiper Telescope of the University of Arizona Observatories maintained by the Steward Observatory (see Table 2). Our data set was supplemented by data from the 4*P Coma Morphology Campaign (Samarasinha et al. 2020). The 4*P Coma Morphology Campaign allowed both professional and amateur observers to submit comet images they obtained following provided guidelines. Of these submitted data sets, we have used images from the telescopes/observers provided in Table 2. It is important to note that these observations were provided by observers following a similar set of instructions, but with diverse instrumentation and filters. The images from the 4*P Coma Morphology Campaign were chosen based on the necessity of time cadence and usability of the images. Occasionally, measurements made at both the

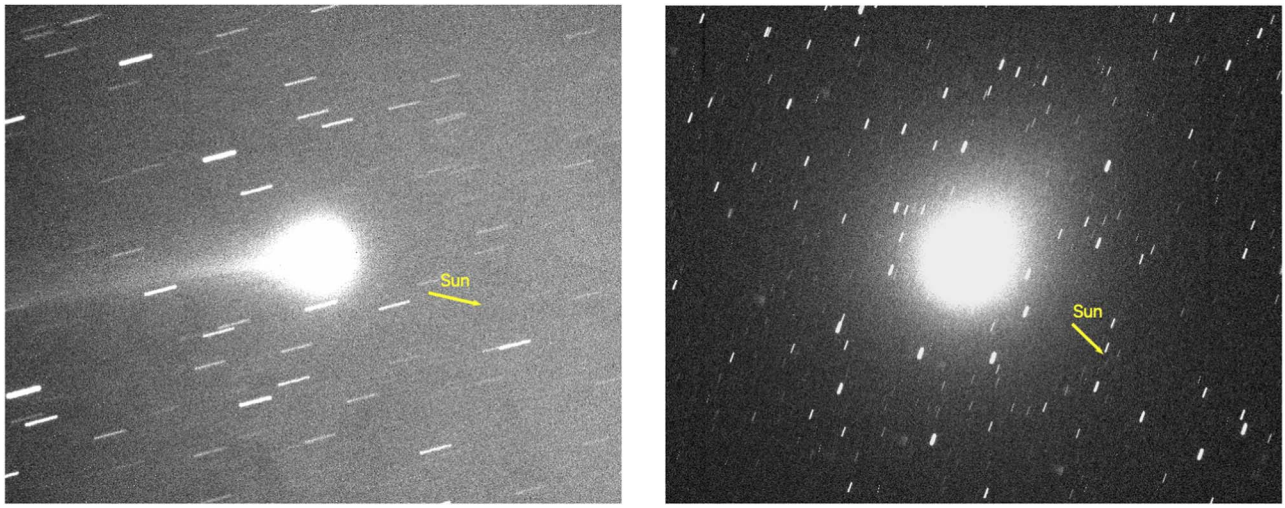

Figure 2. Images of 45P/HMP (left) on 2016 December 28 taken at the Faran telescope and 46P/Wirtanen (right) on 2018 December 9 taken at the Remote Observatory Atacama Desert (ROAD) telescope. Both represent the closest day to perihelion that we have for each comet. The arrows represent the projected solar direction on the plane of the sky, and represent 50,000 km and 10,000 km, respectively. In both images, north is up and east is to the left.

1.54 m Kuiper Telescope and by the 4*P Coma Morphology Campaign were compared to assess systematic errors.

2.2. Photometric Filters

Images were taken at the 1.54 m Kuiper telescope using the HB-BC filter (HB being a reference to Hale–Bopp and BC standing for blue continuum), as described in Farnham et al. (2000), and the Harris-*R* filter. The HB-BC narrowband filter is specially designed to isolate cometary dust in the blue continuum. The Harris-*R* filter, most similar to the Cousins-*R* filter, is a widely used broadband red filter that is dominated by the dust-continuum signal, though might have some limited gas-coma contamination. Having a broadband filter, such as the Harris-*R*, allows us to have a higher signal-to-noise ratio (S/N) than narrowband filters. The HB-BC and Harris-*R* filters were compared on the same date to check for discrepancies in the radial profile slopes, and no significant discrepancies were found. We used both interchangeably, when available, to obtain radial profile slopes, with a preference on the broadband Harris-*R* filter for its higher S/N. As can be seen in Table 2, the ROAD, Savelli, Asiago, Lulin, and Ural telescopes also use a form of the *R* filter. In addition to these two preferred dust filters, some of the observers from the 4*P Coma Morphology Campaign used both clear and light-pollution clear filters. Both of these include almost all the outgassing of the comet in the visible wavelengths, from 400 to 700 nm, with the caveat that the light-pollution filter removes specific wavelength bands usually dominated by Earth's light pollution. Clear filters do not isolate the dust from the gas emissions, however the implications for this will be further examined in Section 3.1 where it is applicable.

2.3. Observations

As described in Section 2.1, the data sets were taken from different telescopes over the globe (see Table 2). Tables 3 and 4 detail observation information, including the dates used, the UT time of the middle of each image (or combined image) used, the heliocentric and geocentric distances, the solar position angle at the time of observations, the projected ranges of radial distance used in the measurements of the radial profiles, and the short name of the telescope from which that specific data were obtained. In summary, we observed 45P/HMP between 2016 December 26 and 2017 March 15 and 46P/Wirtanen between 2018 November 10 and 2019 February 13.

2.4. Data Reduction

Once data were obtained at each telescope, they all went through a basic reduction process that included bias subtraction, flat fielding, and dark subtraction, when necessary. Best efforts were made to measure only the residual dust signal by removing the background flux. Although the lunar illumination was variable over our observation range, it only affected our total flux background and not the shape of the residual cometary signal. Radial profiles were created by measuring the azimuthal median flux as a function of projected distance (ρ) from the nucleus (e.g., Figure 3). Radial profile slopes were measured both for 30° wedges for all azimuths, and for the full 360°. Linear fits were applied and the slopes were recorded. Although the uncertainty is most significant near the edges of the coma, where the overall flux is lower, the errors in the individual data points are a combination of errors in the flat fielding, background removal, and photometric noise. The error in the background removal dominates at greater distances from the nucleus, while the photometric noise dominates closer to the nucleus, as seen in Figure 3, which can then affect the radial profile slope measured. Thus the errors of the slopes of the radial profiles are also a combination of errors in the flat fielding, background removal, and photometric noise.

3. Results

In this section, the flux due to dust continuum as a function of the projected distance from the nucleus, ρ, will be represented in a log–log plot and will be referred to as radial profiles. Figure 4 shows multiple radial profiles over the range of our observed data. The data were plotted to preserve the shape of each curve but not the actual flux measurements, for clarity and comparison.

Table 2
The Telescopes, Observers, and Specific Setups Used in this Paper are Shown Below

Telescope	Observer(s)	Camera	Filter	Field of View (arcmin^2)	Comet Observed	Location	Citation	Short Name
University of Arizona Observatories								
1.54 m Kuiper Telescope	Collaborative program; see Acknowledgments	UA ITL 4K × 4K back-side processed CCD	Harris-*R*, HB-BC	9.7 × 9.7	45P/HMP 46P/ Wirtanen	Tucson, Arizona, USA	Smith (2013)	61″
4*P Coma Morphology Campaign Data Utilized								
ROAD Observatory, 0.4 m (MPC G39)	E. Bryssinck, F.-J. Hambsch	Scientific FLI 16803 4K × 4K	*R*	47 × 47	46P/Wirtanen	San Pedro de Atacama, Chile	Personal communication	ROAD
Osservatorio Astronomico di Savelli, 505 mm	A. Brosio	CCD FLI PL1001 1K × 1K camera	*R*	21 × 21	46P/Wirtanen	Savelli, Italy	Osservatorio Savelli (2020)	Savelli
Stazione Astronomica di Sozzago, 0.4 m	F. Manzini, V. Oldani, P. Ochner, L. R. Bedin	KAF-8300 CCD Moravian G3	Clear	22 × 17	46P/Wirtanen	Sozzago, Italy	Personal communication	Sozzago
Stazione Osservativa di Asiago Cima Ekar, 67/92-cm Schmidt telescope	F. Manzini, V. Oldani, P. Ochner, L. R. Bedin	KAF 16803 CCD Moravian G3. 1.5K Window	Sloan *R*	22 × 22	46P/Wirtanen	Asagio, Italy	Stazione Osservativa di Asiago Cima Ekar (2020)	Asiago
Ritchey–Chretien ($D = 0.4$ m, F/5.4)	A. Maury, J.-B. de Vanssay, J.-G. Bosch	ASCOM_QHY9 CCD 1112 by 832 Camera	Clear	29 × 22	45P/HMP	San Pedro de Atacama, Chile	Personal communication	San Pedro
Faran Observatory ($D = 17''$, F/6.8)	N. Moriya	FLI 16803 4K by 4K Camera	A BAADER UHC-S filter	44 × 44	45P/HMP	Mitzpe Ramon, Negev, Israel	Moriya (2020)	Faran
Lulin Observatory ($D = 41$ cm, F/8.4)	Z.-Y. Lin	Andor Tech CCD 2K by 2K camera	*R*	27 × 27	45P/HMP	Jungli City, Taiwan	Lulin Observatory (2020)	Lulin
Master-Ural	V. Krushinsky, O. Ivanova	Apogee Alta U16 4K by 4K camera	*R*	30 × 30 (cropped)	45P/HMP	Kourovka, Russia	Lipunov et al. (2010)	Ural

Table 3
Dates on which Radial Profiles were Measured for 45P/HMP

45P/Honda–Mrkos–Pajdušáková						
Date	UT Time	r[a] (au)	Δ[b] (au)	Solar Position Angle (degree)	ρ[c] ($\times 10^3$ km)	Telescope
2016-12-26	0:45	−0.54	−0.82	258.1	4.7–79	San Pedro
2016-12-28	16:00	−0.54	−0.77	257.4	3.3–43	Faran
2017-01-09	10:30	0.57	−0.52	253.4	3.0–30	Lulin
2017-02-06	21:50	0.92	−0.10	112.9	0.2–6	Lulin
2017-02-08	12:45	0.94	−0.09	119.2	0.2–4	61″
2017-02-09	12:00	0.95	−0.09	116.4	0.2–7	61″
2017-02-10	12:30	0.97	−0.08	112.7	0.2–6	61″
2017-02-16	10:30	1.05	0.11	81.3	0.3–11	61″
2017-02-16	21:30	1.06	0.11	79.0	0.5–33	Lulin
2017-02-23	20:50	1.16	0.19	47.1	0.9–69	Lulin
2017-02-27	19:45	1.21	0.24	26.6	1.1–68	Lulin
2017-03-07	7:00	1.32	0.34	347.2	2.1–32	61″
2017-03-15	16:20	1.43	0.47	321.4	5.0–56	Ural

Notes. The telescopes' short names are referenced in Table 2. The negative values for the heliocentric/geocentric distances represent the preperihelion/preperigee distances.
[a] Heliocentric distance.
[b] Geocentric distance.
[c] Projected radial distance range measured.

Table 4
Dates on which Radial Profiles were Measured for 46P/Wirtanen

46P/Wirtanen						
Date	UT Time	r[a] (au)	Δ[b] (au)	Solar Position Angle (degree)	ρ[c] ($\times 10^3$ km)	Telescope
2018-11-10	5:20	−1.14	−0.22	197.6	0.9–135	ROAD
2018-11-13	8:45	−1.13	−0.21	201.1	0.7–51	Savelli
2018-11-15	5:35	−1.12	−0.20	202.3	2.0–129	ROAD
2018-11-23	5:00	−1.09	−0.16	209.0	1.3–41	ROAD
2018-11-28	4:45	−1.07	−0.13	212.9	0.5–110	ROAD
2018-11-30	4:40	−1.07	−0.12	214.6	0.5–50	ROAD
2018-12-04	20:15	−1.06	−0.10	219.1	0.3–59	Sozzago
2018-12-09	3:00	−1.06	−0.09	225.9	0.2–18	61″
2018-12-09	4:00	−1.06	−0.09	226.0	0.9–85	ROAD
2018-12-21	5:00	1.06	0.08	312.5	0.2–14	61″
2018-12-26	17:15	1.07	0.10	349.9	0.3–23	Asiago
2018-12-29	7:00	1.08	0.11	0.3	0.3–19	61″
2019-01-05	6:00	1.10	0.14	17.4	0.4–25	61″
2019-01-20	10:00	1.17	0.23	22.1	0.6–22	61″
2019-01-23	7:45	1.19	0.25	20.2	0.6–23	61″
2019-02-08	3:30	1.30	0.37	2.1	0.9–39	61″
2019-02-13	7:30	1.34	0.41	354.9	1.0–35	61″

Notes. The telescopes' short names are referenced in Table 2. The negative values for the heliocentric/geocentric distances represent the preperihelion/preperigee distances.
[a] Heliocentric distance.
[b] Geocentric distance.
[c] Projected radial distance range measured.

3.1. Comet 45P/HMP

Azimuthally medianed radial profile slopes of 45P/HMP taken for the dates in Table 3 are shown in Figure 5. Radial profiles slopes were measured from two different observatories on 2017 February 16 to confirm the relationship between 4*P Coma Morphology Campaign data and the 1.54 m Kuiper Telescope data (Figure 5, 47 days after perihelion). For each date, radial profile slopes were also measured in azimuthal directions every 30° wedge starting from north.

Figure 5 shows a continuous increase in the radial profile slopes from preperihelion through perihelion to postperihelion. The slope goes from much steeper than the fountain model expectation (Section 1.2), at -1.81 ± 0.20 at 5.24 days preperihelion, to much shallower at -0.35 ± 0.16 at 74.41 days postperihelion. It is important to note that the first two data points were taken when the comet was 0.82 au from Earth and with clear filters rather than an *R* filter. The geocentric distance of these data points causes the inner coma to be

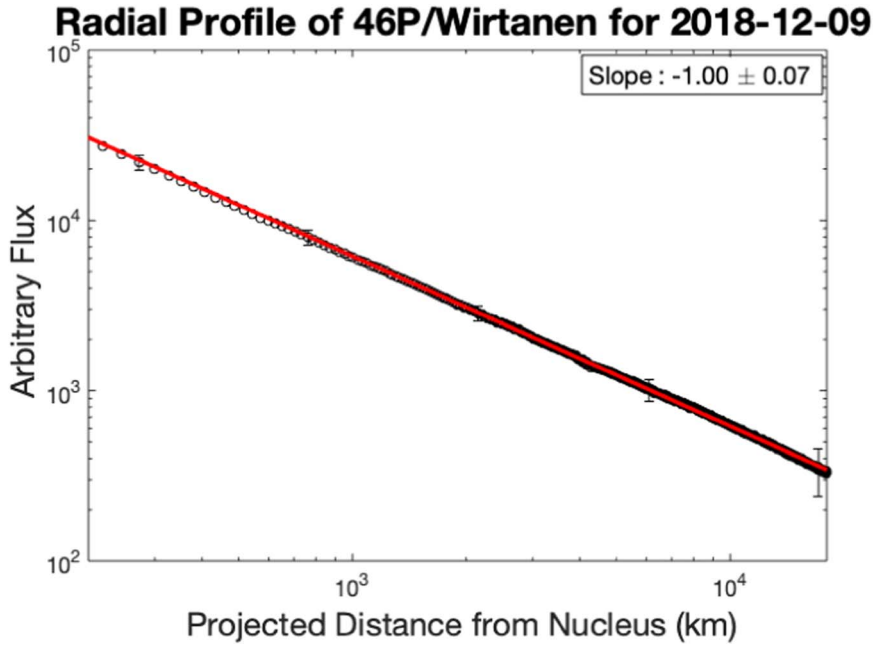

Figure 3. Azimuthally medianed radial profile for 46P/Wirtanen for 2018 December 9 showing five representative error bars for total flux measurements. As visible, the error bars in individual flux measurements are not as important for fitting the slope. The small bump at about 4×10^3 in this radial profile is caused by the CCD imperfections that could not be removed in the reduction process. The red line shows the fit.

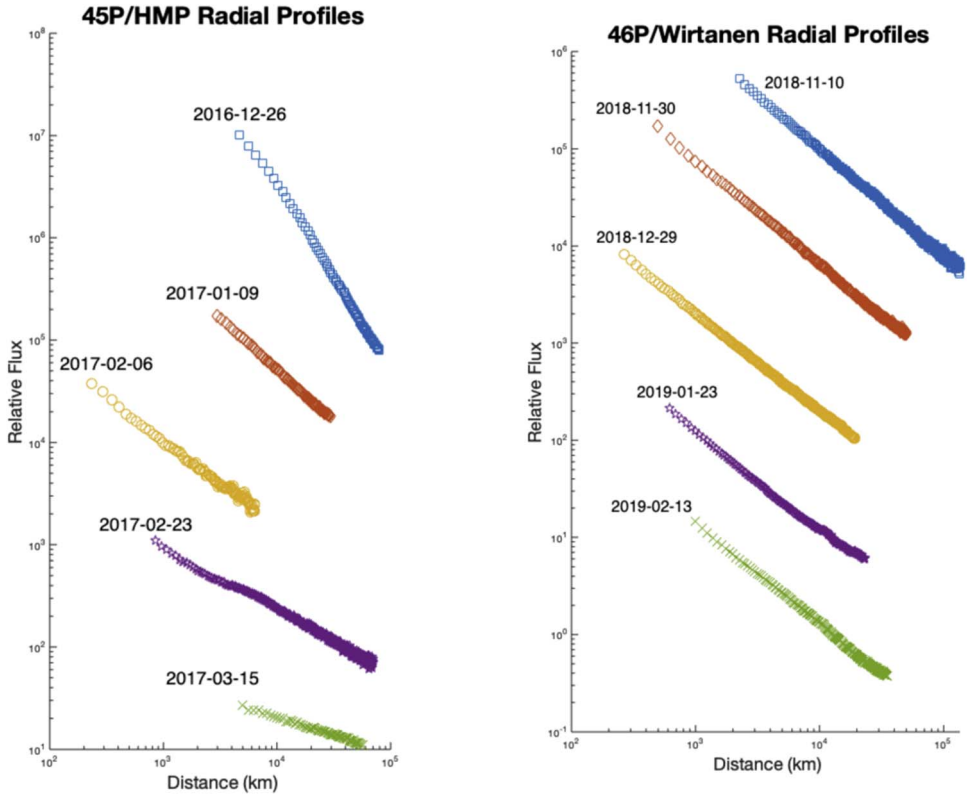

Figure 4. Radial profiles for five dates for comet 45P/HMP (left) showing the shallowing of the slope over the observation range and comet 46P/Wirtanen (right) showing a constant slope over the observation range.

indistinguishable from the outer coma. Additionally, since we are not specifically isolating the dust, we expect gas contamination. However, the major gas contaminants, typically C_2, C_3 and CN, are chemical daughter or granddaughter products and therefore create a radial profile slope shallower than -1, especially close to the nucleus, then become steeper as they dissociate. Hence, the measured slopes corresponding to the clear filter data are upper estimates since they are partially contaminated by the gas.

Additionally, from Figure 4, it is possible to notice that a potentially different radial profile slope could be measured for different distances from the nucleus. We have created distance

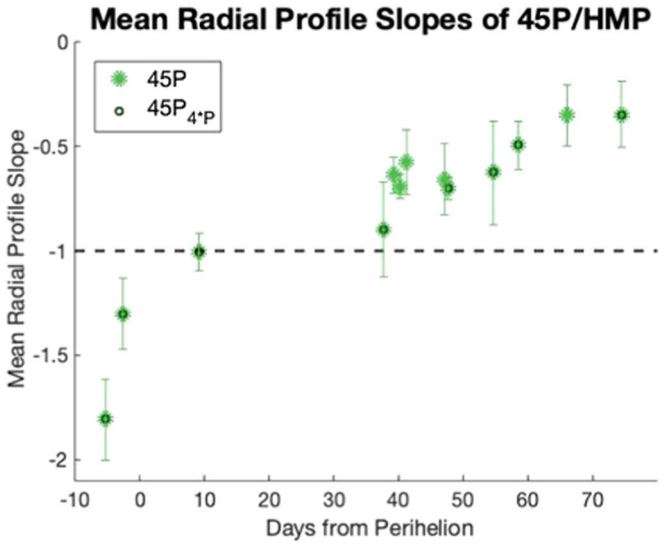

Figure 5. Azimuthally medianed radial profile slopes of 45P/HMP vs. days from perihelion showing a clear shallowing in the slope. The steady-state fountain model is represented with a dashed line. Data points with a green circle represent those images taken by the 4*P Coma Morphology Campaign (Samarasinha et al. 2020).

bins in which we measured the radial profile, when it was feasible to do so for our images. The distance from the nucleus bins were as follows: 10^2–10^3 km, 10^3–10^4 km, and 10^4–10^5 km. Figure 6 shows the results from the azimuthally medianed radial profile slopes binned by distances. Data are not available for each bin on each day primarily due to different geocentric distances and different image sizes. See Table 3 for the specific distances measured. For the six dates for which we have measurements in the 10^2–10^3 km bin, the median profile slope is steeper than for the 10^3–10^4 km distance bin by 0.09 ± 0.08, whereas, the radial profile slope is shallower for the 10^3–10^4 km distance bin than it is for the 10^4–10^5 km distance bin by of 0.33 ± 0.16 for preperihelion and 0.04 ± 0.05 postperihelion. It is important to note, however, that the differences in local slopes binned by distance compared with the unbinned profile slopes, as shown in Figure 6, are comparable to the 1σ uncertainty and must be considered to be only marginally significant.

We also analyzed the azimuthal variation of the radial profile slope. Specifically, we can analyze the slope at different azimuthal directions from the projected solar position angle. We plot the difference between the median slope and the slope of a 30° wedge as a function of the offset from the solar position angle. The offset is calculated as $\mathrm{PA} - \mathrm{PA}_{\odot}$, where PA is the position angle measured from north counterclockwise, and the $\mathrm{PA}_{\odot}$ is the sky-plane-projected solar position angle as given by the JPL Horizons On-Line Ephemeris System (JPL Solar System Dynamic Group 2021).

Figure 7 shows the deviation from the median radial profile slopes versus solar position angle offset. When we look at specific dates, there might be some slight azimuthal discrepancies, but, in general, there is no correlation with $\mathrm{PA}_{\odot}$ offset. This mostly constant deviation from the median radial profile slopes throughout different azimuthal directions suggests that our radial profile slopes measured are a good representation of the radial profile slope each day and are not significantly influenced by jet features, the dust tail, nor radiation pressure.

To confirm the presence, or lack thereof, of significant radial features, we model a dust coma numerically as a circularly symmetric radial profile of the measured median radial profile slope for a specific image. We then divide the original observed image by the modeled dust coma to reveal underlying features, similar to Samarasinha & Larson (2014). This allows us to compare the variations in the radial profile slopes with the physical features we are able to observe. Figure 8 shows the standard reduced image and the same image divided by a circularly symmetric radial profile. There appears to be a sunward feature visible in this enhancement technique. Its significance is discussed in more detail in Section 4.4.

3.2. Comet 46P/Wirtanen

The radial profile slopes of 46P/Wirtanen were measured on 16 different nights, as listed in Table 4, and are presented in Figure 9. Eight of the nights were taken with the 1.54 m Kuiper Telescope while the rest were taken as part of the 4*P Coma Morphology Campaign. Data for the night of 2018 December 9 were analyzed and a radial profile slope was measured from both the 1.54 m Kuiper Telescope and the BRIXIIS telescope as a comparison between our data and the 4*P Coma Morphology Campaign data; no significant discrepancies were found. As for 45P/HMP, we also measured the radial profile slopes at different azimuthal directions every 30° starting from north.

Figure 9 shows the radial profile slopes for 46P/Wirtanen as a function of days from perihelion. For 46P/Wirtanen, the radial slopes do not seem to change greatly over the apparition. If we take the weighted average of all the slopes, we obtained a slope of -1.05 ± 0.05, which is very close to the slope of -1 that we would expect from a spherically expanding fountain model. Measurements were not done at different distances from the nucleus because of the consistency of the slopes as seen in Figure 4.

Figure 10 shows the deviations from the radial profile slopes versus offset from the projected solar position angle (Section 3.1). Comet 46P/Wirtanen seems to have a clear trend in the deviation from the median radial profile slopes centered at 180° from the solar position angle (i.e., the antisunward direction). It appears that the radial profile is shallower, by approximately 0.1 in the antisunward direction. We discuss in Section 4.4 a possible reason for this phenomenon.

4. Discussion

Prior to comparing our results with the relevant literature, it is important to reiterate the specific observing geometries corresponding to our observations. Because of the very close geocentric distances of both comets, we were able to resolve the inner comae in our observations of these comets, something rarely achievable except by spacecraft (for the ranges of ρ probed; see Tables 3 and 4).

Our measurements show comet 45P/HMP changing from a radial profile slope of -1.81 ± 0.20 to -0.35 ± 0.16 from preperihelion to postperihelion. Furthermore, 45P/HMP's radial profile slope seems to be changing, though remains within a 1σ error, with different binned distances from the nucleus of the comet. These are unusual behaviors, which we try to characterize below. For comet 46P/Wirtanen, we obtained a fairly constant radial profile slope of -1.05 ± 0.05

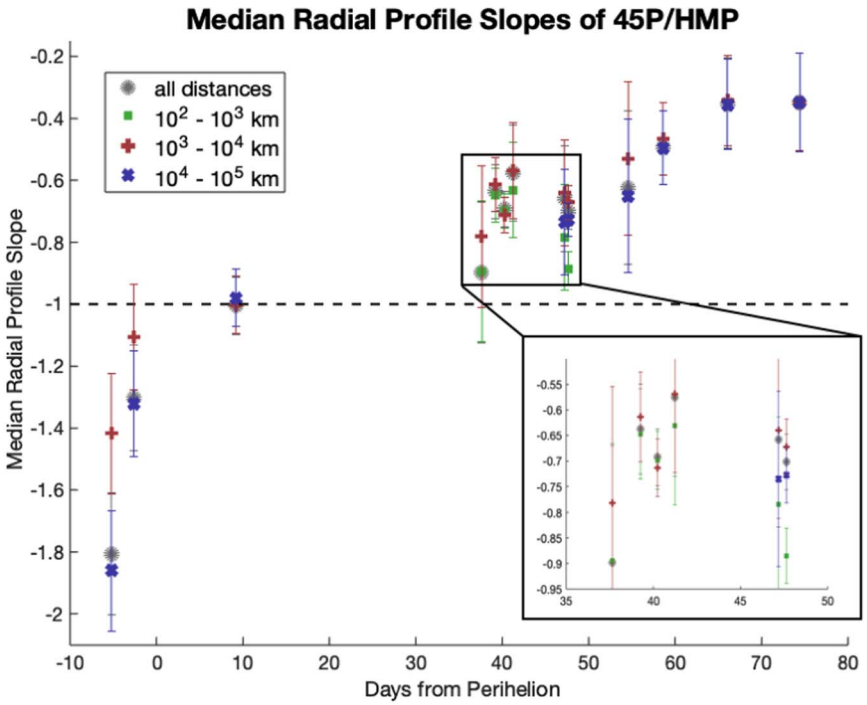

Figure 6. Azimuthally medianed radial profiles binned by distance from the nucleus. The zoom-in panel shows in greater detail the days close to perigee where it might be otherwise hard to see the difference between the distance bins. "All distances" includes data points that might be outside the specific bins present for that specific day but where there were insufficient additional data to obtain a statistically significant result for the additional distance bins.

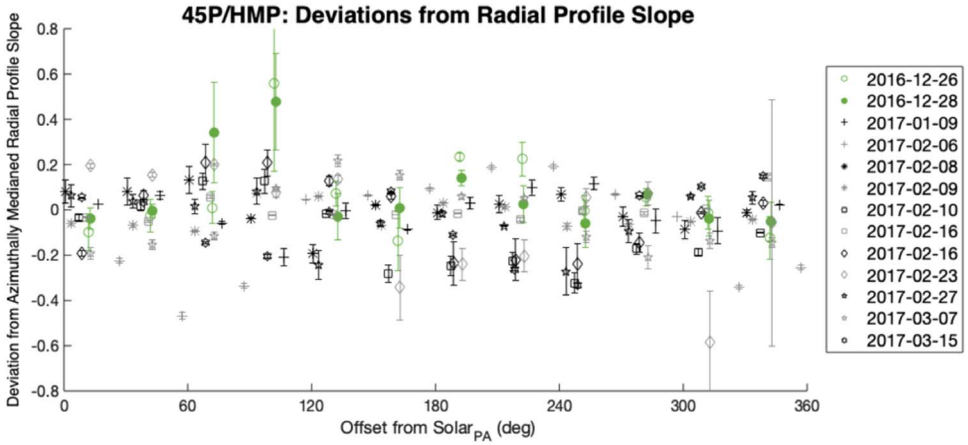

Figure 7. Deviations from azimuthally medianed radial profile slope for 45P/HMP vs. the offset from the solar position angle (PA − $PA_{\odot}$) measured every 30° centered on north. The green markers are preperihelion while the gray markers are the postperihelion measurements. The error bars here represent the error in slope based upon the error on the background measurements.

over a span of 95 days, which suggests a steady-state coma following the fountain model (Samarasinha & Larson 2014). However, comet 46P/Wirtanen's radial profile slopes do appear to have an azimuthal dependence. Coulson et al. (2020) measured the continuum-emission radial profile at 850 μm for comet 46P/Wirtanen, and found a slope of −1 as close as at least 630 km from the nucleus for the dates of 2018 December 14–20. This shows that our measurements are consistent with independently obtained measurements at different wavelengths representing larger grains.

4.1. Dust Fragmentation of 45P/HMP

Our results highlight the importance of closely analyzing the dust radial profile slopes and understanding the behavior of the dust and the dust–gas coupling properties (see Section 1). When analyzing the radial profile slopes, it is important to consider the water-production rate, dust-grain sizes, and grain cohesiveness. As water-production rates increase, both the dust-production rate and potentially the dust particle sizes in the coma increase. Larger, fluffier grains are more likely to fragment early due to gas pressures, while small cohesive grains will fragment less easily. In the case of fragmenting fluffier grains, we can expect a shallowing of the dust profile slope, while cohesive, unfragmenting grains would tend to follow a slope of −1. As clearly visible in Figure 5, comet 45P/HMP has a radial profile slope going from very steep to very shallow. Factors that would cause a deviation from the $1/\rho$ dust radial profile from the fountain model include (1)

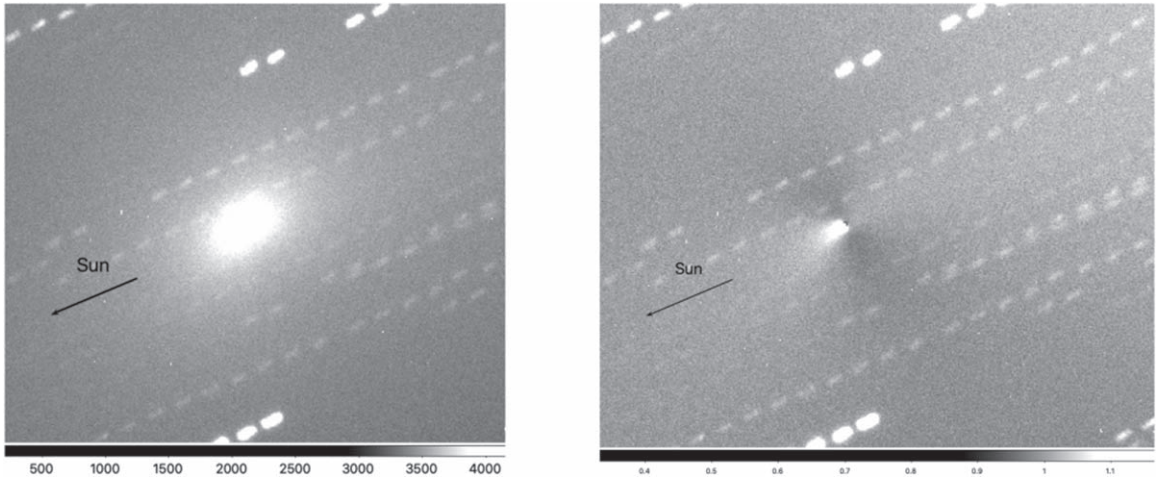

Figure 8. Left: standard reduced image of 45P/HMP on 2017 February 10. Right: same image divided by a circularly symmetric radial profile model of the azimuthally medianed radial profile slope measured, showing a sunward feature. In both images, the arrow length represents 2000 km, and north is up and east is to the left.

asymmetry in the gas-production distributions (e.g., jet features), (2) multiple velocity distributions for the dust, (3) variable grain-size distributions, (4) variable dust-production rates, (5) radiation pressure effects, especially farther out from the nucleus, and (6) the evolution of dust with radial distances from the nucleus. This last point is particularly important because of processes such as grain fragmentation and sublimation in an icy-grain halo (see Section 1.1), which has an important implication for 45P/HMP.

Combi et al. (2020) show that 45P/HMP is reasonably symmetric in the gas-production rates pre- and postperihelion, and, if we assume that dust has to be driven by some type of gas behavior, we find that our asymmetry pre- and postperihelion in Figure 5 to be of importance. Dust velocity dispersion, variable grain-size distribution, and variable dust-production rates are all beyond the scope of this paper, and therefore can only be speculated on when trying to find a possible explanation.

Equation (4) from Mueller et al. (2013) provides a method for calculating the turn-back distance of dust grains in the comae of comets due to radiation pressures. For comet 45P/HMP specifically, we can use our current knowledge to calculate a best estimate of this distance. The utilized parameters are as follows: (1) the grain outflow velocity is a minimum of 15 $\mathrm{m\,s^{-1}}$ for centimeter-sized grains but much higher for micron-sized grains(E. Howell 2021, personal communication), (2) the heliocentric distances are mentioned in Table 3, (3) the range of solar phase angle are 17.°1 at 0.54 au preperihelion and 167.°7 at 1.43 au postperihelion (JPL Solar System Dynamic Group 2021), (4) the ratio of radiation pressure to gravitational pressure being ∼0.01 for grains of a few microns in size (Burns et al. 1979), and (5) we can assume a sky-plane angle of 45° as an average since we have no further knowledge of the subject. With these parameters, we obtain a turn-back distance ranging from 250 to 6500 km. This is a lower estimate from a minimum velocity, and actual distances might be higher. Additionally, factors such as total gas-production rates, grain sizes, and albedo of the dust were not accounted for specifically. While some grains are likely to reach a turn-back distance, on average, since our velocity is physically going to be higher for smaller grains, there is a high likelihood that a majority of our grains will not turn back within our field of view, and those grains will not have a major role in the radial profile.

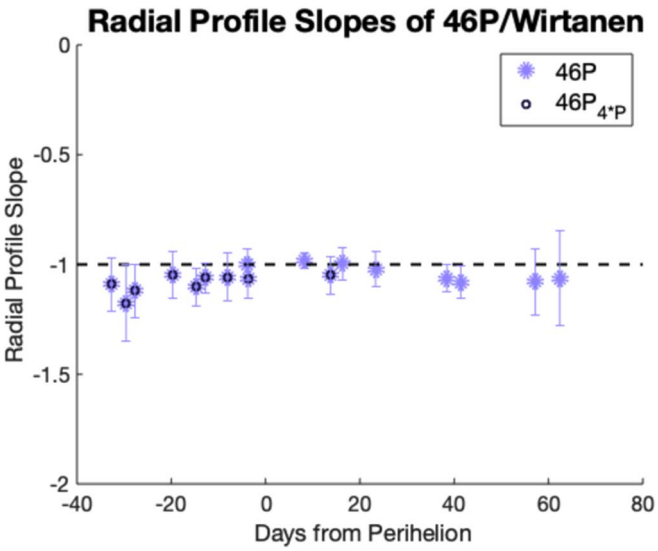

Figure 9. Azimuthally medianed radial profile slopes of 46P/Wirtanen vs. days from perihelion showing a fairly constant slope. The steady-state fountain model is represented with a dashed line. Data points with a blue circle represent those images taken by the 4*P Coma Morphology Campaign (Samarasinha et al. 2020).

Thus, if we assume that other factors are in play, we can try to understand the behavior we see in Figure 5 by first understanding the behavior of an optically thin symmetric dust coma. As explained in Jewitt & Meech (1987), for an optically thin symmetric coma generated by a constant source with constant-velocity dust grains that have retained their scattering properties, the radial surface-brightness profile is given by $B(\rho) = K/\rho$, where K is a constant. A simple way to look at the behavior of dust in the inner coma is to represent radial brightness as a function of projected distance in a log–log plot. This allows the slope of the radial profile to become

$$m = \frac{d \log B(\rho)}{d \log \rho}, \quad (1)$$

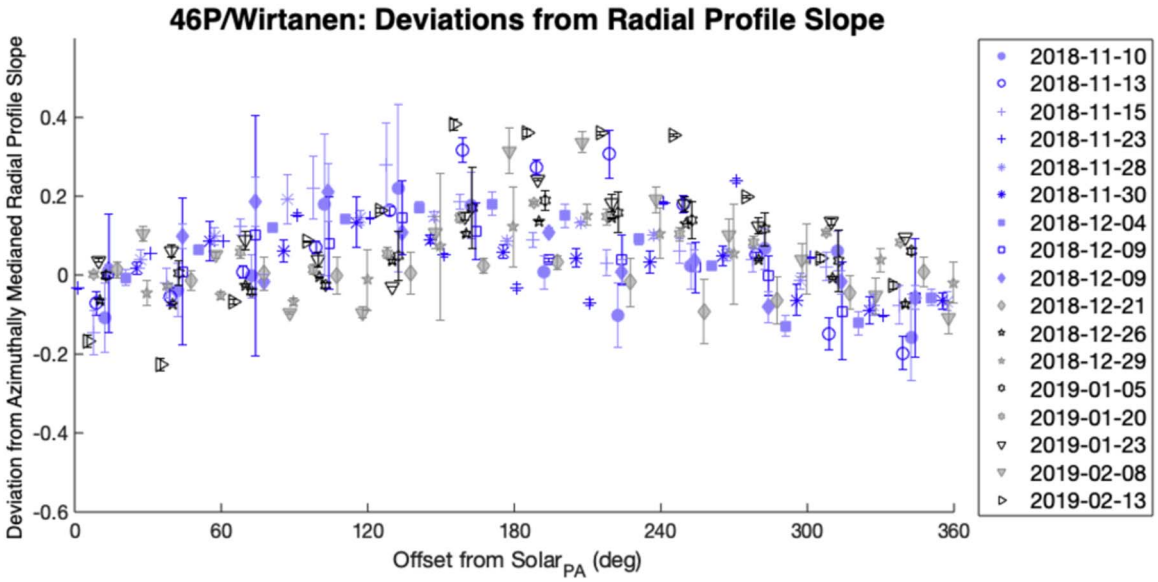

Figure 10. Deviations from median radial profile slope for 46P/Wirtanen vs. the offset from the solar position angle (PA − $PA_{\odot}$) measured in 30° wedges starting from north. The blue markers are preperihelion while the gray markers are the postperihelion measurements. The error bars here represent the error in slope based upon the error of the background measurements.

where the steady-state symmetrical case described above would lead to $m = -1$ (Jewitt & Meech 1987). Deviations from $m = -1$, such as a grain-fragmentation scenario, would make the slope shallower (less negative) while an icy-grain-halo scenario would cause a steeper slope (more negative). In the case of grain fragmentation, we would increase the amount of reflected sunlight progressively farther from the nucleus by increasing the net grain cross-section. This increases the brightness of the coma farther away from the nucleus. Conversely, in the case of icy grains, as we go farther from the nucleus, we would be losing total mass of dust, and thus effective cross-section. The total albedo of the grains would also be reduced, as the composition changes from icier material (high albedo) to dustier material (low albedo). This decreases the overall brightness of the coma farther away from the nucleus. Multiple processes can occur simultaneously in the dust expansion (e.g., fragmentation, sublimation, and albedo changes) with the net effect on the radial profile slope being dependent on which effect dominates the observed properties.

One possibility to explain the reduction in radial profile slope for 45P/HMP would be gradual changes to the types of dust grains leaving the comet, essentially creating a variable grain-size distribution. We can imagine large icy grains originally leaving the comet as it approaches perihelion, then, those having been depleted, and the dust production becoming weaker as the comet moves away from the Sun, only the small nonicy grains being released and continuing to fragment. The extremely steep radial profile slope preperihelion would suggest that a very rapid process existed to reduce the total flux from dust grains as they moved farther from the nucleus.

Dust fragmentation is a possibility, especially if much larger icier grains are present preperihelion than postperihelion. If the slope continues to become shallower, it suggests that the grains are becoming more friable, but, however, might contain less ice. Furthermore, the shallowing of the radial profile slope with distance for preperihelion of 0.32 ± 0.16 from 10^3–10^4 km to 10^4–10^5 km suggests an even more complex evolution of the grain in the coma, such as a mix of icy and dusty grains, or simply extremely icy, larger grains, that fragment into smaller still icy grains. The postperihelion change in radial profile slope in these distance bins seem minimal enough that such a complex process might have stopped by then and possibly only nonicy grains might be at play during postperihelion.

4.2. Acceleration of Dust Grains Due to Outgassing

Before the dust grains reach their terminal velocity and are still being accelerated by gas pressure, we expect a steep brightness profile near the nucleus. A rough estimate was made by Jewitt & Meech (1987) based on mostly water production at 1 au from the Sun to calculate an acceleration zone, X_a:

$$3r_n \leqslant X_a \leqslant 30r_n, \tag{2}$$

where r_n is the nucleus radius. From radar images, an estimate of 45P/HMP's diameter is 1.3 km (Lejoly & Howell 2017) while 46P/Wirtanen is approximately 1.4 km in diameter (E. Howell 2021, personal communication), giving us 2 km $\lesssim X_a \lesssim$ 20 km for both comets. In our observations, our best resolution at the optimal geometry gives us 25 km pixel^{-1}, and is unable to resolve the rapid acceleration of dust by the sublimating ices in the nucleus.

The issues of acceleration depend on total gas-production rate, grain size, and albedo, which is where the order of magnitude comes into play. This is only a rough estimate and it is possible to have residual effects of that acceleration at distances of 100 km. The slight steepening of the slope of 0.09 ± 0.08 seen near perigee (about 40–50 days postperihelion) in Figure 6 could be explained by the dust still being accelerated by gases leaving the nucleus.

Since dust and gas are coupled near the nucleus, the behavior of gas itself can also affect the dust radial profile. In Combi et al. (2020), power laws for water production of both comets are fitted to their data. Though not symmetric about perihelion for either comet, there does not seem to be any odd behavior that could cause the radial profile slope measurements we

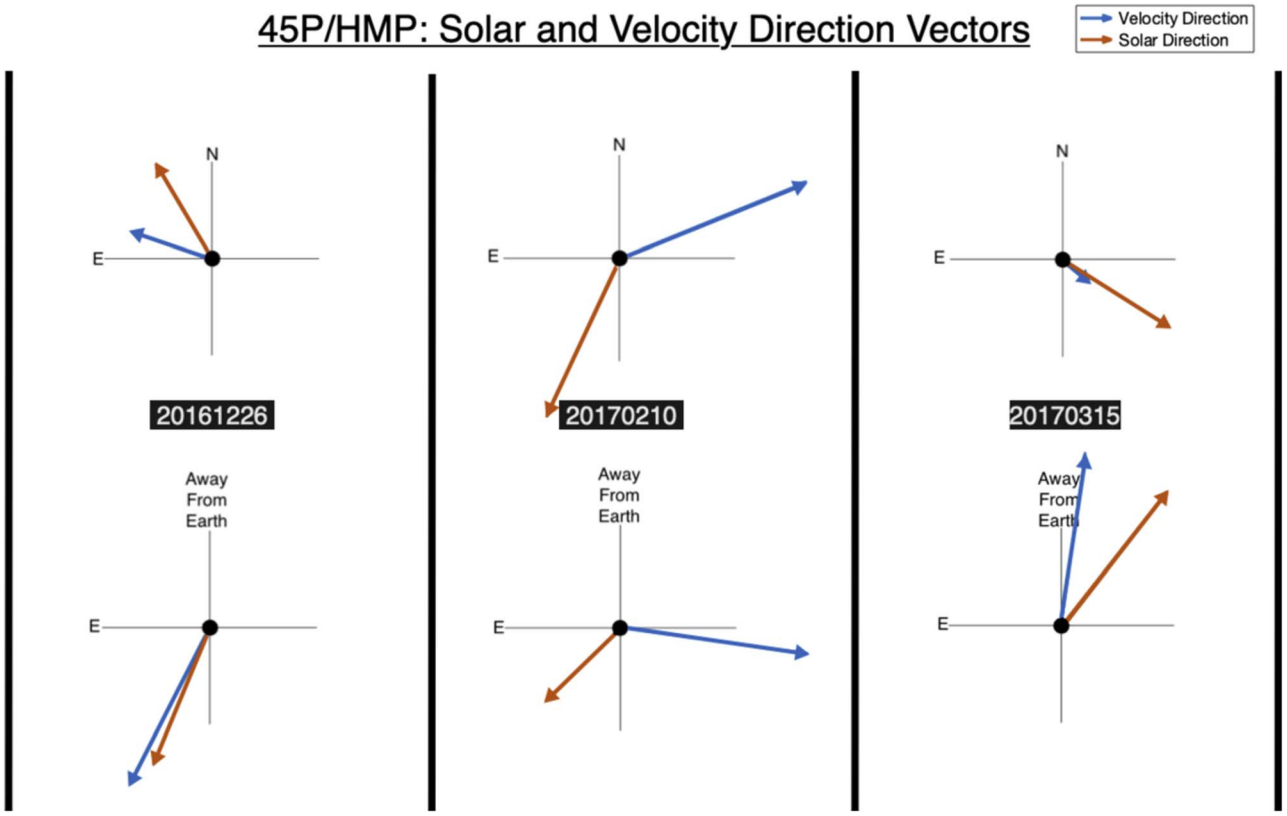

Figure 11. The velocity and solar direction vectors as seen in the plane of the sky (top) and rotated 90° from the plane of the sky (bottom) for 45P/HMP on our first observation (left), our observation closest to perigee (middle), and our last observation (right). Projections north and east represent our sky plane.

observe for 45P/HMP (Figure 5), such as sudden brightening, nucleus fragmentation, etc. For 45P/HMP, Dello Russo et al. (2020) measure a postperihelion water-production rate of $Q(H_2O) = (2.81 \pm 0.25) \times 10^{27}[r^{-3.83\pm0.18}]$ molecules s^{-1}; it is also stated that there might be significant variability in H_2O production on timescales of days and even hours. This could cause slope changes on small time frames, but not a global shallowing trend as visible in our data. When looking at the production rates of other gas molecules (OH, CN, C_3, and C_2), all appear to have a similar, slightly decreasing trend from 40 to 70 days postperihelion (Moulane et al. 2018). Therefore, it does not appear that the gas behavior alone can explain our shallowing of the radial profile slopes for 45P/HMP.

4.3. Dust Grain Behavior's Effects on Radial Profiles

The size, density, composition, outflow velocity, and overall behavior of dust grains can greatly affect the radial profiles, both globally and in specific azimuthal directions on a specific date. All of these parameters are difficult to constrain; however, we have some indication of grain sizes and velocities. From the Arecibo Observatory radar measurements of both 45P/HMP and 46P/Wirtanen, "radar skirts" were detected, which indicates coma grains of at least 4 cm (E. Howell 2021, personal communication). Specifically, for 46P/Wirtanen, we can also determine that these grains must have been moving at a minimum velocity of 15 $m\,s^{-1}$ away from the nucleus (E. Howell 2021, personal communication). In accordance with the radar measurements, Zheltobryukhov et al. (2020) also found evidence of a circumnucleus halo of dust, suggesting either diffuse outgassing or the merge of multiple weak jets. For the large grains to be important in our measurements of radial profile slopes, there would have to be a very massive, ongoing flux of large particles. It is more likely that the smaller grains dominate the coma in visible light.

$Af\rho$, the product of albedo, A, a filling factor, f, and the projected radial distance, ρ, on the plane of the sky (A'Hearn et al. 1984), is representative of dust-production rates. For 45P/HMP, $Af\rho$ peaks 50 days postperihelion at 33 cm in the R_c filter (comparable to the Harris-R filter) and then decreases afterwards (Moulane et al. 2018). The peak in $Af\rho$ at 50 days postperihelion found by Moulane et al. (2018) potentially matches with a steepening of the radial profile slope, however their time baseline does not cover as extensive a range as ours does. An increase in the dust production at the nucleus would temporarily cause the radial profile slope to be steeper than −1, corresponding to the small dip around 50 days postperihelion that is visible in Figure 5.

As explained in Section 4.1, grain fragmentation can cause a steepening or a shallowing of the radial profile slope depending on the composition of the grain. Depending on the icy-grain environments, such as quick fragmentation of icy grains, sublimation of icy grain, or even icy-grain mantling, for example, could result in different radial profiles provided that the icy grains survive long enough (e.g., Beer et al. 2006; Markkanen & Agarwal 2020; Davidsson et al. 2021). This, combined with the radar measurements, suggests that if icy grains were present in either 45P/HMP, 46P/Wirtanen, or both, an icy dust halo could be present, creating a shallowing of the radial profile slope. Comets 45P/HMP and 46P/Wirtanen have very different radial profile slopes, which suggests that the two comets have vastly different dust environments in their inner comae.

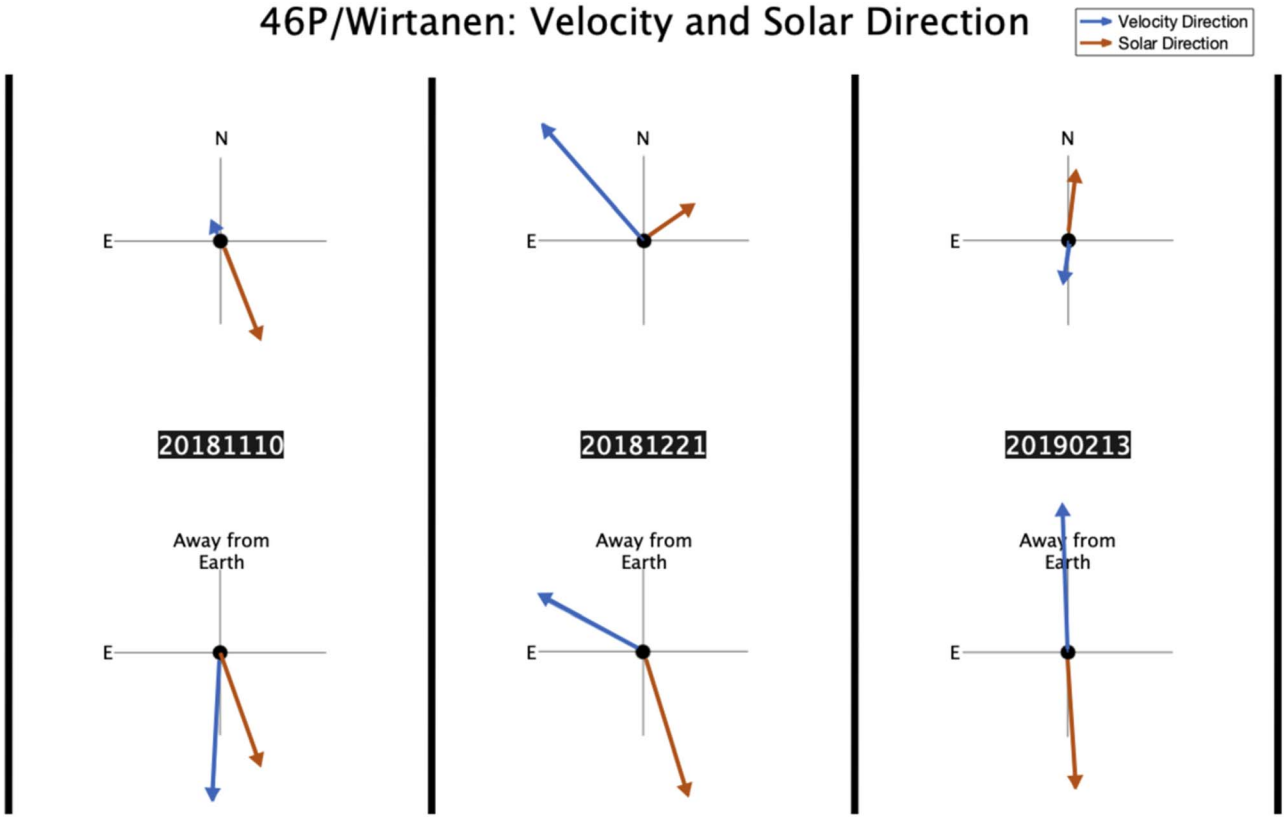

Figure 12. The velocity and solar direction vectors as seen in the plane of the sky (top) and rotated 90° from the plane of the sky (bottom) for 46P/Wirtanen on our first observation (left), our observation closest to perigee (middle), and our last observation (right). Projections north and east represent our sky plane.

4.4. Solar Position Angle Correlation

The solar position angle changes more than 180° over the course of our observations for both comets (Tables 3 and 4). Thus, it was logical to show the dependence of the radial profiles with respect to the solar position angles as shown in Figures 7 and 10. Comet 45P/HMP does not show any significant correlation with azimuthal offsets from the solar position angle. However, 46P/Wirtanen does show an overall shallower slope in the antisunward direction and a steeper slope in the sunward direction. This trend is visible in both the pre- and postperihelion data. Figures 11 and 12 show that the Sun is in the direction of the Earth for most of the 46P/Wirtanen encounter, but closer to the sky plane for 45P/HMP. This suggests that there might be more prominent changes in radial profiles due to the tail projection onto the sky plane for comet 46P/Wirtanen. We also see a weaker tail feature in Figure 8 for 45P/HMP than in Figure 13 for 46P/Wirtanen. A detailed grain model, outside the scope of this observational study, that includes grain fragmentation, radiation pressures, different grain compositions, etc., would be necessary to further understand the outcomes of radial profiles with respect to behaviors of grain environments.

Essentially, in 46P/Wirtanen, we are looking at more material from the antisunward (tail) direction at each ρ, so the grains' total cross-section builds up faster potentially due to grain fragmentation, and we would observe a shallowing of the slope simply due to the projected tail feature. Additionally, because the solar phase angle is smaller, we would also observe more contamination from the direction reversal of the sunward direction moving grains toward the tailward direction due to radiation pressures.

Contrarily, the weak antisunward (tail) feature of 45P/HMP is more often closer to the sky plane (see Figure 8), so any potential change to the radial profile would be much smaller, and in our data potentially be below our noise threshold. Additionally, Figure 8 shows a weak sunward feature which does not seem to affect the radial profile slope visible in Figure 7. This could simply imply that the grains in the sunward feature are behaving similarly to the grains in the rest of the coma in terms of their radial distribution, even though there might simply be larger flux present.

The tailward-direction radial profile slope shallowing of 46P/Wirtanen is most likely not caused by only radiation pressure in the coma. Essentially, in a spherically expanding coma subjected to radiation pressure, for the sunward direction, as you move progressively away from the nucleus, more and more grains amass because of the decrease of velocity due to radiation pressure, causing a shallowing of the slope. In the tailward direction, as you move progressively away from the nucleus, the grains have had more time to accelerate due to radiation pressure, and keep accelerating, causing a steepening of the slope. This is the opposite behavior that we observe in 46P/Wirtanen. However, since we know that 46P/Wirtanen has large grains, which are less affected by radiation pressure, they have more time to disintegrate and essentially amass farther out. Depending on the mechanism of fragmentation of large grains (if they were to fragment), there could be more generations of smaller grains (i.e., micron sized) consistently, resulting in an increase in grain cross-section, thus causing a shallower slope.

However, it is unlikely that the tailward shallowing of 46P/Wirtanen is caused by cm-sized grains moving along the orbit

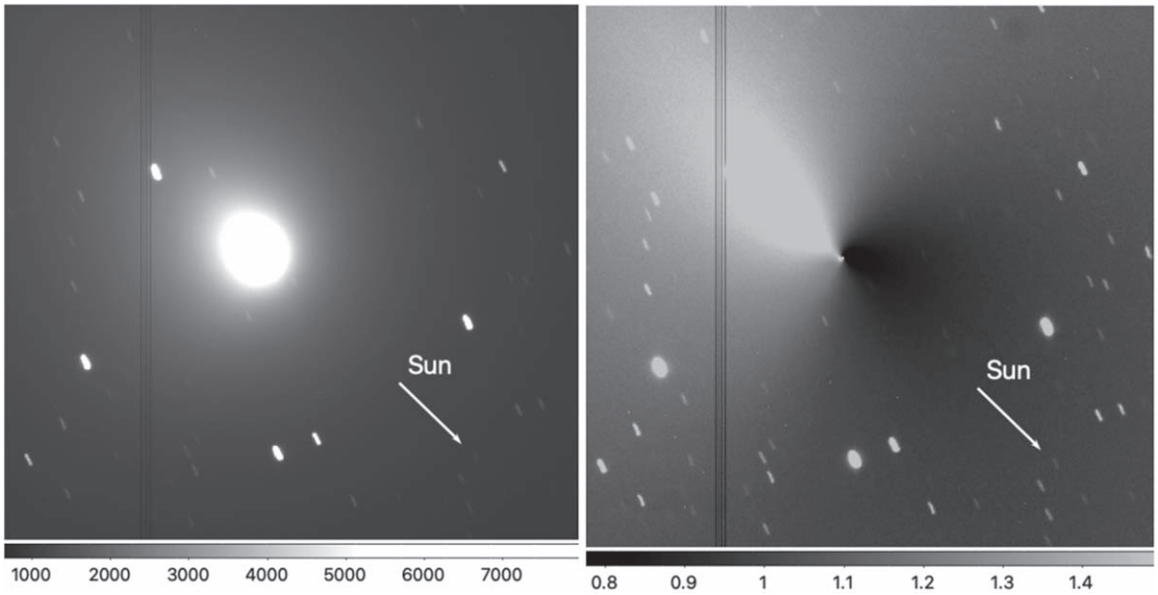

Figure 13. Left: standard reduced image of 46P/Wirtanen on 2018 December 9. Right: same image divided by a circularly symmetric radial profile model of the median radial profile slope measured showing a strong antisunward feature (i.e., the tail). In both images, the arrow length represents 2000 km and north is up, east is to the left.

of the comet forming a dust trail. As seen in Figure 12, the velocity direction does not align with the solar direction (or their converse), thus the feature in the tailward direction is not correlated with the orbital direction.

5. Conclusion

We find that the radial profile slopes of comets 45P/HMP and 46P/Wirtanen, measured over 79 and 95 days, respectively, have different temporal behaviors. Comet 45P/HMP has a radial profile slope that becomes shallower with time, starting at -1.81 ± 0.20 preperihelion and ending at -0.35 ± 0.16 postperihelion during our observations. Resolution of the inner coma, near perigee, suggest we may have been able to resolve the zone of interaction when the dust and gas were still coupled. Surprisingly, the radial profile slope near perihelion appears to be closest to -1. This suggests that there might be different dust processes occurring preperihelion and postperihelion, such as a change in grain composition or friability. Additionally, the transition between different processes seems gradual, suggesting that it is not caused by a single short event. On the other hand, 46P/Wirtanen's radial profile slope appears fairly constant at -1.05 ± 0.05. This suggests that there is a constant behavior for the dust expansion of 46P/Wirtanen, possibly a steady-state expansion of the dust coma, as described in the fountain model (see Section 1.2), and, at this point, processes more complicated need not be invoked for explaining the azimuthally medianed radial profiles of 46P/Wirtanen.

The two most interesting results from our analysis are the shallowing of 45P/HMP's slope over the apparition and the shallowing of the radial profile slope of 46P/Wirtanen in the tailward direction. Possible explanations for 45P/HMP's behavior are as follows:

1. a peak in $Af\rho$ near 50 days postperihelion and decrease right after it would cause a gradual shallowing of the radial profile slope; or
2. a progressive change in the type of dust grains from large icy grains preperihelion to small nonicy grains postperihelion.

On the other hand, the tailward shallowing of the slope for 46P/Wirtanen, which is not present in 45P/HMP, is most likely caused by a combination of the following:

1. a projection angle effect of the dust tail away from the observer's direction; and
2. larger grains ejected in the tailward direction that are not accelerated as quickly due to radiation pressure; they might eventually fragment, cause an increase in micron-sized grains, and in turn increase the net dust-grain cross-section.

Such a difference in radial profile slopes between comets 45P/HMP and 46P/Wirtanen suggests that the two have vastly different dust environments in their inner comae. This indicates that at least the upper layer of the two comets' nuclei are significantly different. Our results imply that a combination of the surface properties, total gas production, and the distribution of the source regions all play a role in the two comets' dust environments.

We would like to thank everyone who participated in the data-gathering process. This includes all students from the Lunar and Planetary Laboratory course PTYS 495B/595B (Fall 2018). We would also like to thank the additional organizers of the 4*P Campaign: Matthew Knight (United States Naval Academy) and Tony Farnham (University of Maryland). We would like the thank the Steward Observatory technical staff for the amount of time they dedicated to this project. Finally, we would like to thank the SSO grant No. NNX16A670G (Walt Harris) and the NESSF grant No. 80NSSC18K1241 (Cassandra Lejoly; P.I.: Walt Harris) for allowing this work to be completed. We would also like to thank the Slovak Academy of Sciences grant No. VEGA 2/0023/18 (Oleksandra Ivanova) and the Slovak Research and

Development Agency under the Contract no. APVV-19-0072 (Oleksandra Ivanova).

ORCID iDs

C. Lejoly https://orcid.org/0000-0003-0165-7701
W. Harris https://orcid.org/0000-0002-8378-4503
N. Samarasinha https://orcid.org/0000-0001-8925-7010
B. E. A. Mueller https://orcid.org/0000-0001-6194-3174
A. Springmann https://orcid.org/0000-0001-6401-0126
T. Kareta https://orcid.org/0000-0003-1008-7499
B. Sharkey https://orcid.org/0000-0003-1383-1578
J. Noonan https://orcid.org/0000-0003-2152-6987
L. R. Bedin https://orcid.org/0000-0003-4080-6466
O. Ivanova https://orcid.org/0000-0001-7285-373X
V. Krushinsky https://orcid.org/0000-0001-9388-691X

References

A'Hearn, M. F., Schleicher, D. G., Millis, R. L., et al. 1984, AJ, 89, 579
Altwegg, K., Balsiger, H., Bar-Nun, A., et al. 2016, SciA, 2, e1600285
Beer, E. H., Podolak, M., & Prialnik, D. 2006, Icar, 180, 473
Belton, M. J. & Members of the Deep Impact Science Team 2006, AAS/DPS Meeting Abstracts, 38, 17.08
Brownlee, D. 2014, AREPS, 42, 179
Burns, J. A., Lamy, P. L., & Soter, S. 1979, Icar, 40, 1
Combi, M. R., Mäkinen, T., Bertaux, J.-L., et al. 2020, PSJ, 1, 72
Coulson, I. M., Liu, F., Cordiner, M. A., et al. 2020, AJ, 160, 182
Davidsson, B. J. R., Birch, S., Blake, G. A., et al. 2021, Icar, 354, 114004
Dello Russo, N., Kawakita, H., Bonev, B. P., et al. 2020, Icar, 335, 113411
Eddington, A. S. 1910, MNRAS, 70, 442
Farnham, T. L., Knight, M. M., Schleicher, D. G., et al. 2021, PSJ, 2, 7
Farnham, T. L., Schleicher, D. G., & A'Hearn, M. F. 2000, Icar, 147, 180
Festou, M. C. 1981, A&A, 95, 69
Hanner, M. S., & Bradley, J. P. 2004, in Comets II, ed. M. C. Festou, H. U. Keller, & H. A. Weaver (Tucson, AZ: Univ. Arizona Press), 555
Haser, L. 1957, BSRSL, 43, 740
Ivanovski, S. L., Zakharov, V. V., Della Corte, V., et al. 2017, Icar, 282, 333
Jewitt, D. C., & Meech, K. J. 1987, ApJ, 317, 992
JPL Solar System Dynamic Group 2021, NASA/JPL Horizons On-Line Ephemeris System, http://ssd.jpl.nasa.gov/?horizons
Lamy, P. L., Toth, I., Jorda, L., et al. 1998, A&A, 335, L25
Lejoly, C., & Howell, E. 2017, CBET, 4357
Lipunov, V., Kornilov, V., Gorbovskoy, E., et al. 2010, AdAst, 2010, 349171
Lulin Observatory 2020, 0.41-meter Telescope, http://www.lulin.ncu.edu.tw
Markkanen, J., & Agarwal, J. 2020, A&A, 643, A16
Moriya, N. 2020, Faran Observatory, 17" Telescope, https://faran-observatory.net
Moulane, Y., Jehin, E., Pozuelos, F. J., et al. 2018, A&A, 619, A156
Mueller, B. E. A., Samarasinha, N. H., Farnham, T. L., et al. 2013, Icar, 222, 799
Osservatorio Savelli 2020, L'Osservatorio—Parco Astronomico Lilio Savelli, https://www.astrosavelli.it/losservatorio/
Samarasinha, N., Mueller, B. E. A., Knight, M., Farnham, T. L., & Harris, W. 2020, 4*P Coma Morphology Campaign, https://www.psi.edu/41P45P46P
Samarasinha, N. H., & Larson, S. M. 2014, Icar, 239, 168
Smith, P. 2013, Basic Information About Mont4K Used at the Kuiper Telescope, http://james.as.arizona.edu/psmith/61inch/CCDbasicinfo.html
Stazione Osservativa di Asiago Cima Ekar 2020, http://archive.oapd.inaf.it/asiago/3000/3100.html
Weissman, P., Morbidelli, A., Davidsson, B., et al. 2020, SSRv, 216, 6
Weissman, P. R., Asphaug, E., & Lowry, S. C. 2004, in Comets II, ed. M. C. Festou, H. U. Keller, & H. A. Weaver (Tucson, AZ: Univ. Arizona Press), 337
Zheltobryukhov, M., Zubko, E., Chornaya, E., et al. 2020, MNRAS, 498, 1814